Supporting Information

Valence-Regulated Metal Doping of Mixed-Halide Perovskites to Modulate Phase Segregation and Solar Cell Performance

Long Hu[1,2#], Xinwei Guan[3#], Tao Wan[2#], Chun-Ho Lin[2], Shanqin Liu[4], Renbo Zhu[2], Weijian Chen[5], *Yin Yao[6],* Chien-Yu Huang[2], Lin Yuan[1], Shamim Shahrokhi[2], Dewei Chu[2]*, Claudio Cazorla[7*], Junfeng Chen[8], Jack Yang[2]*, Jiabao Yi[3], Shujuan Huang[1]*, Tom Wu[2]*

[1] School of Engineering, Macquarie University Sustainable Energy Research Centre, Macquarie University, Sydney, NSW, 2109, Australia

[2] School of Materials Science and Engineering, University of New South Wales (UNSW), Sydney, NSW, 2052 Australia

[3] Global Innovative Centre for Advanced Nanomaterials, School of Engineering, College of Engineering, Science and Environment, The University of Newcastle, Callaghan, NSW, 2308 Australia

[4] School of Chemistry and Chemical Engineering, Henan Institute of Science and Technology, Xinxiang, Henan, 453003 P. R. China

[5] School of Photovoltaics and Renewable Energy Engineering, University of New South Wales (UNSW), 2052 Australia

[6] *Electron Microscope Unit, Mark Wainwright Analytical Centre, UNSW Sydney, Sydney, New South Wales, 2052, Australia*

[7] Departament de Física, Universitat Politècnica de Catalunya, Campus Nord B4-B5, E-08034 Barcelona, Spain

[8] R&D Center, Shanghai Institute of Ceramics, Chinese Academy of Sciences, Shanghai 201899.

Email: d.chu@unsw.edu.au; claudio.cazorla@upc.edu; jianliang.yang1@unsw.edu.au; shujuan.huang@mq.edu.au; tom.wu@unsw.edu.au

1. Experimental section:

1.1 Chemicals and Materials:

All following chemicals were purchased from Sigma-Aldrich: lead bromide ($PbBr_2$; 99.999%), cesium iodide (CsI, 99.999), silver iodine (AgI, 99.99%), zinc iodine (ZnI_2, 99.99%), antimony iodine (SbI_3, 99.99%), Spiro-MeOTAD (Sigma, 99%), [6,6]-Phenyl C61 butyric acid methyl ester (Sigma, 99.5%), gold (Au, 99.99%), anhydrous chlorobenzene (CB, 99.8%), anhydrous dimethylsulfoxide (DMSO, 99.9%). Tin oxide nanoparticle solution is from Alfa Aesar (SnO_2, 15% in H_2O colloidal dispersion). All chemicals were used as received without further purification unless mentioned.

1.2 Mixed halide perovskite precursor solution preparation:

Four types of mixed halide perovskite films (i.e., undoped and AgI-, ZnI_2-, and SbI_3-doped $CsPbIBr_2$) were deposited by using one-step antisolvent spin-coating method. 1 M $CsPbIBr_2$ precursor solution was prepared by dissolving 1.468 g $PbBr_2$ and 1.04 g CsI into 4 mL DMSO solvent under continuous stirring at 70 ^oC for 3 h, then, this uniform solution was filtered and divided into four equal parts with 1 ml for each. Subsequently, AgI, ZnI_2 and SbI_3 were loaded into DMSO to form uniform solutions with concentrations of 0.1 M, respectively. Then, 0.1 ml of AgI, ZnI_2, and SbI_3 additive solutions were added into 1 ml pristine $CsPbIBr_2$ solution separately to obtain the heteroatom incorporated solutions with the additive molar concentration of 1.0% for each, while 0.1 ml pure DMSO solvent was added into control solution to form pristine solution.

1.3 Mixed halide perovskite films and solar cell fabrication:

Patterned ITO glasses were cleaned using detergent, de-ionic water, isopropanol, and acetone, then O_2 plasma was used to treat the ITO surface for 1 min. Diluted SnO_2 nanoparticle solution with a weight concentration of 2.5% was spin-coated on ITO glasses and annealed on a hotplate at 120 ^oC for 30 min in ambient condition. Before halide perovskite deposition, SnO_2 films were treated with O_2 plasma for 1 min. Then the SnO_2 nanoparticle substrates were transferred to a glove box filled with nitrogen. Four types of precursor solutions were spin-coated on ITO/SnO_2 substrate at 1500 rpm for 15 s and then at 4500rpm/45 s. In the spin-coating process of the second step, after 30 s, anti-solvents methyl acetate was dropped rapidly. Then, mixed halide perovskite films were annealed at 150 ^oC for 10 min. For solar cell fabrication, Spiro chlorobenzene solution was spin-coated on halide perovskite films at 4000 rpm for 30 s. Finally, 100 nm of Au electrode were deposited by thermal evaporation through a shadow mask to form 0.075cm^2 devices under a vacuum of 2×10^{-6} mbar.

2. Characterizations:

An I-V tester equipped with a Keithley 2400 source meter was employed to test the current density-voltage (J-V) under the standard 1 sun illumination from an AM 1.5G solar simulator. EQE measurements were performed utilizing an IEC 60904-8 international standard certified EQE equipment (Solar Cell Scan 100, Zolix Instruments Co. Ltd.). Field emission scanning electron microscopy (SEM), FEI Nova NanoSEM 230 was used to acquire SEM images. Steady-state PL measurements were conducted by WITec Alpha300 confocal Raman spectroscopy to investigate the PL behavior under a 532 nm laser with a fixed light excitation intensity of 1 mW/cm^2. UV-Vis absorption spectra were acquired using a U-4100 spectrophotometer (Hitachi). The perovskite films' charge transport property was characterized using a probe station connected to a Keithley 4200 Semiconductor Parametric Analyzer. The PL decay traces and fluorescence images were measured on a Micro Time

200 (Picoquant) confocal microscope using the TCSPC technique with one-photon excitation of a 470 nm laser. Two identical single-photon avalanche photodiode (APD) detectors were used; therefore, dual-channel signals were recorded simultaneously. All PL measurements were undertaken at room temperature. XPS and UPS measurements were conducted by a VG ESCALAB MK2 system with monochromatized Al Kα radiation under a pressure of 5.0×10^{-7} Pa. The XRD was carried out on a MPD (PANalytical) Xpert Multipurpose X-ray diffraction system using Cu Kα radiation (λ = 1.5406 Å).

3. Theoretical Calculations

3.1 First-principles calculations based on density functional theory

First-principles calculations based on density functional theory (DFT)[1] were carried out in which the PBEsol exchange-correlation energy functional[2] was used as it is implemented in the VASP software.[3] The projector-augmented wave method (PAW)[4] was employed to represent the ionic cores by considering the following electronic states as valence: Cs 5*s* 5*p* 6*s*; Pb 6*p* 5*d* 6*s*; I 6*s* 5*p*; Br 5*s* 4*p*; Ag 5*s* 4*d*; Zn 4*p* 3*d*; Sb 5*s* 5*p*. The Grimme's D3 scheme[5] was employed for a better treatment of the dispersion interactions in the system. An energy cutoff of 650 eV and a Monkhorst-Pack k-point grid of 8×6×4 were used for integrations within the Brillouin zone, leading to total energies converged to within 1 meV per atom. Atomic relaxations were concluded when the forces in the atoms were all below 0.005 eV/Å. The employed simulation supercell contained 40 atoms and was constructed as a √2x2x2 √2 replication of the usual 5-atoms perovskite unit cell (Figure 6a). Different arrangements of the I and Br ions were explored with the finding that the lowest energy was obtained when the Br ions occupied the equatorial plane positions of the halide-ion octahedra and the I ions the corresponding apical positions (Figure 6a). Such a relative Br/I ion position arrangement was fixed for the rest of calculations. A Pb ion was substituted by a Ag, Zn or Sb ion in order to simulate the doped $CsPbIBr_2$ systems. The electronic properties of the the different systems were estimated with the accurate screened hybrid exchange-correlation functional HSE06.[6]

In order to determine the possible values of the chemical potential of the atomic species forming the $CsPbIBr_2$ perovskite, we have proceeded as follows. First, we considered the stability condition:

$$\mu_{Cs} + \mu_{Pb} + 3\mu_{Br} = \Delta H^f (CsPbBr_3) \quad [1]$$

where the equality $\mu_I = \mu_{Br}$ has been assumed and $\Delta H^f (CsPbBr_3)$ is the formation enthalpy of $CsPbBr_3$ calculated with DFT methods (i.e., -6.646 eV per formula unit -f.u.-). The chemical potentials are referred to the calculated energies of the pure bulk compounds. The formation enthalpy of the competing phases CsBr and $PbBr_2$ provide additional bounds to the chemical potentials, namely:

$$\mu_{Cs} + \mu_{Br} < \Delta H^f(CsBr) \quad [2]$$

$$\mu_{Pb} + 2\mu_{Br} < \Delta H^f(PbBr_2) \quad [3]$$

where $\Delta H^f(CsBr)$ and $\Delta H^f(PbBr_2)$ are the formation enthalpies of bulk CsBr and $PbBr_2$ calculated with DFT methods (i.e., -3.767 and -2.732 eV/f.u., respectively). With Eqs.[1]-[3], we can determine the phase diagram and chemical potential bounds:

$$\mu_{Pb} + 2\mu_{Br} > -2.879 \text{ eV} \quad [4]$$

$$\mu_{Pb} + 2\mu_{Br} < -2.732 \text{ eV} \quad [5]$$

as it appears shown in Figure 6c.

The formation energy of each native defect (E^f) with a charge state q, was estimated with the well-known formula:[7, 8]

$$E^f = E_{tot}(X^q) - E_{tot}(\text{bulk}) - \Sigma n_i \mu_i + qE_F + \Delta^q \quad [6]$$

where $E_{tot}(X^q)$ is the total DFT energy of a $CsPbIBr_2$ supercell containing the native defect X with charge state q and E_{tot}(bulk) the total DFT energy of a pristine $CsPbIBr_2$ supercell of the same size. The parameter n_i is the number of atomic species i that is added to ($n_i>0$) or removed from ($n_i<0$) the supercell to create the defect X. The parameter μ_i is the chemical potential of the atomic species i, E_F the Fermi level (or, equivalently, the chemical potential of the electrons) as referred to the valence band maximum, and Δ^q a finite-size correction term for charged defects.[7, 8]

3.2 Random Sampling of the Solid Solutions

To model the solid solutions of $Cs(Pb_{0.95}X_{0.05})IBr_2$ ($X=Ag^+$, Zn^{2+}, Sb^{3+}), we start from the 26 optimized $(2 \times 2 \times 2)$ supercell structures of $CsPbIBr_2$ from our previous work,[9] and replacing 1 out of all 8 Pb atoms in each structure to build atomistic models at the composition of $Cs(Pb_{0.875}X_{0.125})IBr_2$, using the same random sampling algorithm for building the atomistic models of $CsPbIBr_2$. This leads to a total of 570 atomistic configurations for $Cs(Pb_{0.875}X_{0.125})IBr_2$ across all three X dopants investigated here.

3.2 Structural Optimization with Density Functional Theory (DFT)

We optimized both the atomic positions and lattice parameters at the Perdew-Burke-Ernzerhof (PBE) level of theory using the VASP code.[10, 11] Default energy cut-off for the projector-augmented-wave (PAW) at NORMAL accuracy are used throughout the optimizations, which are terminated when the residue forces are below 10^{-4} eV $Å^{-1}$.[12] Monkhorst-Pack k-point sampling is used at a uniform grid spacing of 0.04 $Å^{-1}$ in the reciprocal space. All calculations are carried out without the inclusion of spin-polarization.

3.4 Room-Temperature Structural and Electronic Dynamics

To further understand how the structural and electronic dynamics of $CsPbIBr_2$ are affected by B-site cation mixings, we performed *ab initio* molecular dynamic (MD) simulations on the optimized structures for $Cs(Pb_{0.875}X_{0.125})IBr_2$ ($X=Ag^+$, Zn^{2+}, Sb^{3+}) with the *most positive* ΔH_{demix}, which correspond to structures with the least thermodynamic driving force for halogen segregation. MD simulations are performed on a $(2 \times 1 \times 1)$ supercell of the optimized static structure at 300 K using a single K-point at NORMAL accuracy setting. The GW version of the pseudopotential is used to achieve better electronic convergence. Each system is first equilibrated for 500 fs to the target temperature with

the velocity scaling algorithm. Production run for a 10 ps trajectory with 1 fs step size is subsequently performed under the NVT ensemble together with an Andersen thermostat at a collision frequency of 0.5. MD snapshots are collected every 1 fs for structural analysis, whereas electronic density-of-states (DOS) calculations are performed on MD frames extracted every 10 fs along the trajectory. To further expedite the calculations, DOS at Γ-point only is calculated, from which the band gap energies are extracted.

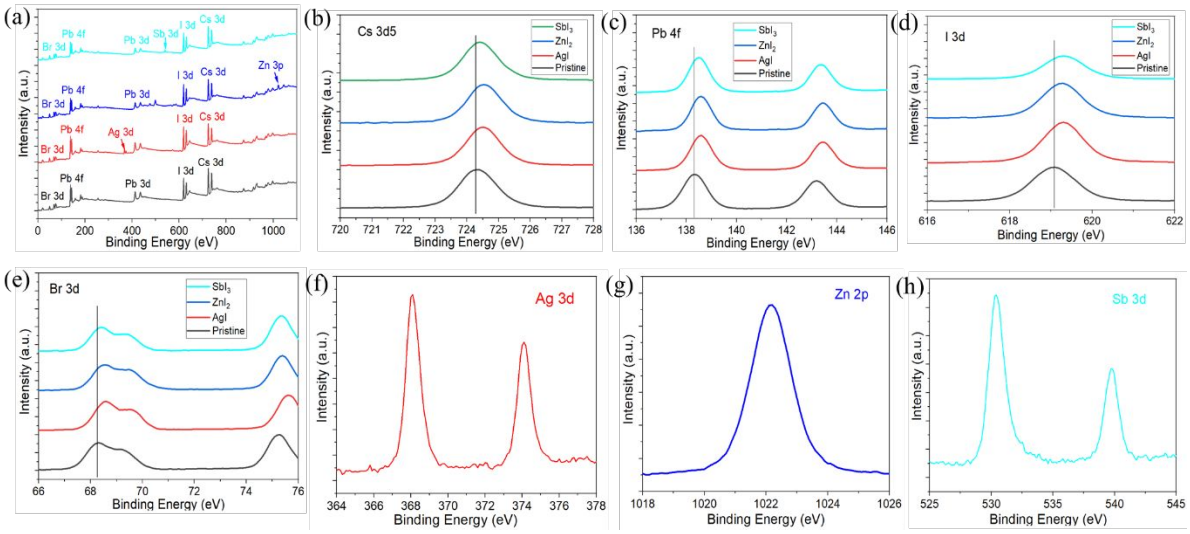

Figure S1. (a) XPS whole spectra of four types of mixed halide perovskite films. XPS core spectra of (b) Cs 3d5 (c) Pb 4f (d) I 3d (e) Br 3d (f) Ag 3d, (g) Zn 3p and (h) Sb 3d of mixed halide perovskite films.

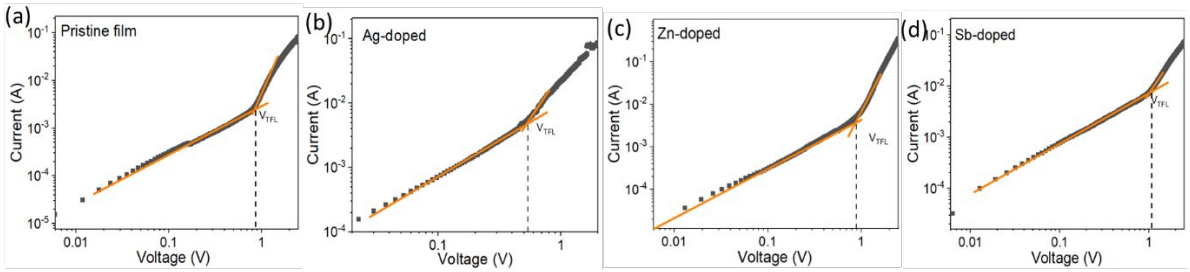

Figure S2. Space charge limited current curves of (a) pristine, (b) Ag-doped, (c) Zn-doped and (d) Sb-doped $CsPbIBr_2$ perovskite films.

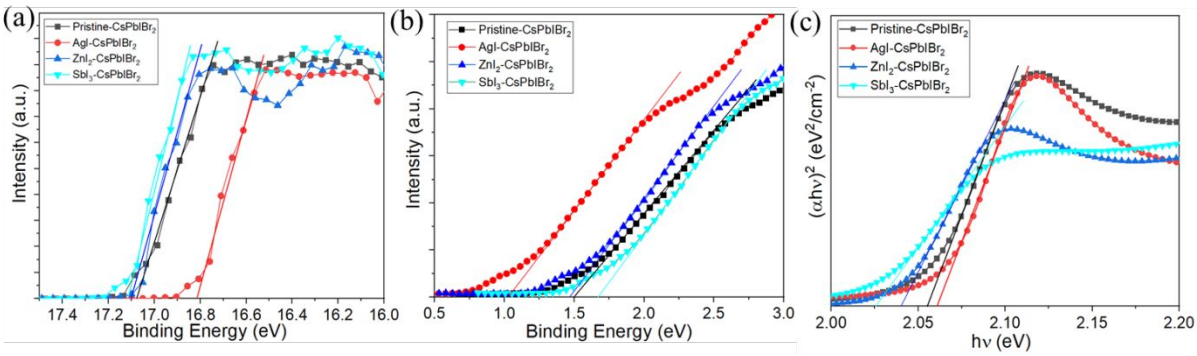

Figure S3. UPS spectra of different perovskite films in the (a) cut-off and (b) valence band edge regions. (c) Bandgap of different perovskite films extracted from the absorption data.

Table S1. Band energy levels measured from 3 spots for each film.

	Fermi Level			VBM			CBM		
Film type	Spot-1	Spot-2	Spot-3	Spot-1	Spot-2	Spot-3	Spot-1	Spot-3	Spot-3
Pristine	-4.12 eV	-4.15 eV	-4.17 eV	-5.62 eV	-5.67 eV	-5.64 eV	-3.58 eV	-3.52 eV	-3.51 eV
AgI	-4.31 eV	-4.29eV	-4.33 eV	-5.54 eV	-5.52 eV	-5.49 eV	-3.48 eV	-3.43 eV	-3.47 eV
ZnI_2	-4.10 eV	-4.14 eV	-4.30 eV	-5.66 eV	-5.62 eV	-5.68 eV	-3.62 eV	-3.61 eV	-3.57 eV
SbI_3	-4.01 eV	-3.98 eV	-4.28 eV	-5.67 eV	-5.62 eV	-5.65 eV	-3.64 eV	-3.60 eV	-3.67 eV

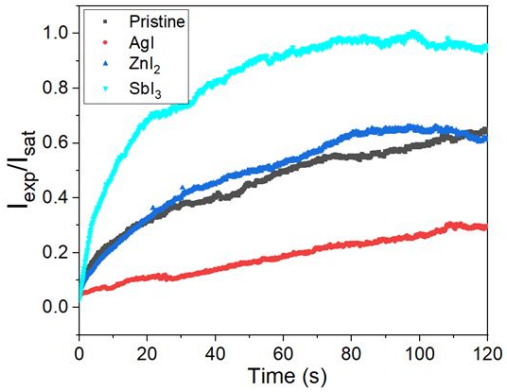

Figure S4. Time-dependent phase segregation level (I_{exp}/I_{sat}) for pristine, AgI-, ZnI_2- and SbI_3-incorporated $CsPbIBr_2$ films.

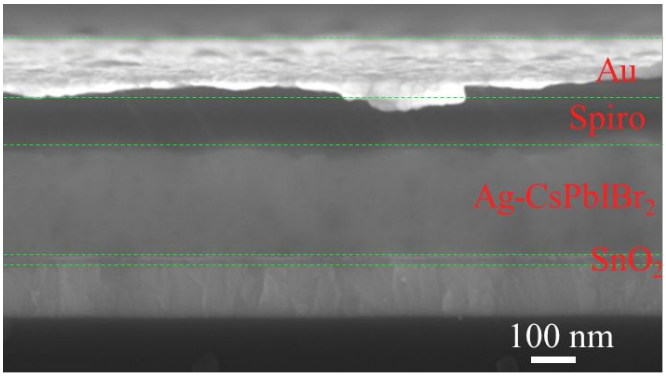

Figure S5. Cross-sectional SEM image of Ag-doped $CsPbIBr_2$ solar cell.

Table S2. The statistics of four types of solar cells (The Champion parameters in parentheses)

Cell types	Voc (V)	Jsc (mA/cm^2)	FF (%)	PCE (%)
Pristine	1.17±0.03 (1.21)	10.1±0.3 (10.6)	70±3 (72)	8.3±0.3 (9.0)
AgI	1.22±0.02 (1.24)	10.9±0.2 (11.1)	73±2 (74)	9.7±0.3 (10.1)
ZnI_2	1.16±0.03 (1.19)	10.0±0.3 (10.4)	67±3 (69)	7.8±0.4 (8.4)
SbI_3	1.12±0.04 (1.15)	9.4±0.4 (9.8)	66±4 (67)	7.0±0.4 (7.6)

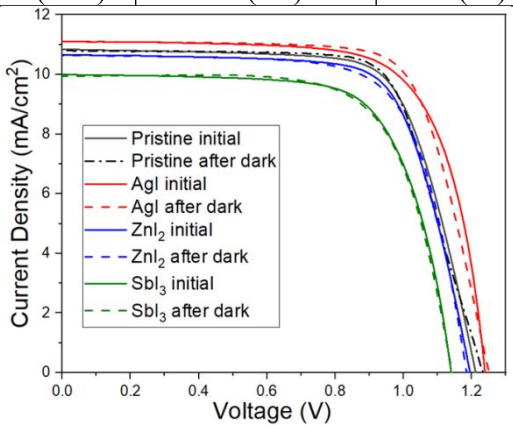

Figure S6. J-V curves of pristine, AgI, ZnI_2, and SbI_3 doped $CsPbIBr_2$ solar cells before continuous illumination and dark storage after continuous illumination.

Reference:

1. Cazorla, C.; Boronat, J., Simulation and understanding of atomic and molecular quantum crystals. *Rev. Mod. Phys.* **2017,** *89* (3), 035003.
2. Perdew, J. P.; Ruzsinszky, A.; Csonka, G. I.; Vydrov, O. A.; Scuseria, G. E.; Constantin, L. A.; Zhou, X.; Burke, K., Restoring the density-gradient expansion for exchange in solids and surfaces. *Phys. Rev. Lett.* **2008,** *100* (13), 136406.
3. Kresse, G.; Furthmüller, J., Efficient iterative schemes for ab initio total-energy calculations using a plane-wave basis set. *Phys. Rev. B* **1996,** *54* (16), 11169.
4. Blochl, P. E., Projector augmented-wave method. *Phys. Rev. B Condens. Matter* **1994,** *50* (24), 17953-17979.
5. Grimme, S.; Antony, J.; Ehrlich, S.; Krieg, H., A consistent and accurate ab initio parametrization of density functional dispersion correction (DFT-D) for the 94 elements H-Pu. *J. Chem. Phys.* **2010,** *132* (15), 154104.
6. Brothers, E. N.; Izmaylov, A. F.; Normand, J. O.; Barone, V.; Scuseria, G. E., Accurate solid-state band gaps via screened hybrid electronic structure calculations. *J. Chem. Phys.* **2008,** *129* (1), 011102.
7. Menéndez, C.; Chu, D.; Cazorla, C., Oxygen-vacancy induced magnetic phase transitions in multiferroic thin films. *Npj Comput. Mater.* **2020,** *6* (1), 1-9.
8. Zhang, X.; Shen, J. X.; Turiansky, M. E.; Van de Walle, C. G., Minimizing hydrogen vacancies to enable highly efficient hybrid perovskites. *Nat. Mater.* **2021,** *20* (7), 971-976.
9. Yang, J.; Wang, Y.; Wu, T.; Li, S., Correlating the composition-dependent structural and electronic dynamics of inorganic mixed halide perovskites. *Chem. Mater.* **2020,** *32* (6), 2470-2481.
10. Perdew, J. P.; Burke, K.; Ernzerhof, M., Generalized gradient approximation made simple. *Phys. Rev. Lett.* **1996,** *77* (18), 3865.
11. Kozlov, A. N.-E. S. M.; Viñes, F.; Illas, F., Electronic-structure-based chemical descriptors:(in) dependence on self-interaction and Hartree-Fock exchange. *Phys. Rev. B* **1996,** *54*, 11169-11186.
12. Kresse, G.; Joubert, D., From ultrasoft pseudopotentials to the projector augmented-wave method. *Phys. Rev. B* **1999,** *59* (3), 1758.